ACS Energy LETTERS

http://pubs.acs.org/journal/aelccp

Full-Space Potential Gradient Driven Charge Migration inside $BiFeO_3$ Photocathode

Bing Tan, Abdul M. Reyes, Eduardo Menéndez-Proupin, Sebastian E. Reyes-Lillo,* Yanbo Li,* and Zemin Zhang*

Cite This: https://doi.org/10.1021/acsenergylett.2c01750

Read Online

ACCESS | Metrics & More | Article Recommendations | Supporting Information

ABSTRACT: Solar−fuel conversion depends on effective collection of photocarriers in the photoelectrode. In practice, however, considerable photocarriers are lost in the bulk through recombination due to the absence of a driving force. To overcome this, herein, a full-space electric field is induced in $BiFeO_3$ photocathodes by building a gradient homojunction through Fermi level engineering. As expected, the $BiFeO_3$ photocathodes with forward electric field show significantly enhanced performance: a state-of-the-art photocurrent of -1.02 mA·cm^{-2} at 0.5 V vs RHE and H_2O_2 production of 380 mmol·(L·m^2)$^{-1}$ within 50 min. First-principles calculations and experimental analysis suggest that the Bi vacancies as shallow acceptors can significantly modulate the Fermi level of $BiFeO_3$. The resulting internal electric field serves as an additional driving force to promote charge collection. This work provides an approach to induce a full-space electric field in semiconductor films through gradient defects modulation, which can be broadly applied to other optoelectronic systems.

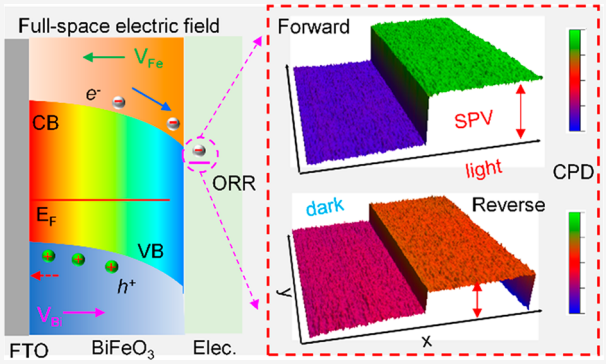

Photoelectrochemical (PEC) synthesis has received growing attention as a green approach to produce hydrogen peroxide (H_2O_2).[1−4] This approach takes advantage of the charge-separation ability of semiconductor−liquid junctions, which provides excited photocarriers to produce H_2O_2 via dioxygen reduction or water oxidation.[5] Despite great efforts, the practical application of PEC H_2O_2 production is still challenging due to severe photocarrier losses through recombination.[6−8] For many emerging photoelectrode materials, photocarrier diffusion length is limited to 10−50 nm and only 10% of photocarriers have been collected.[9,10] Generally, photoelectrodes are separated into a space charge region and a natural region, while recombination majorly (90%) occurs in the natural region due to the absence of a drive force.[11,12] Therefore, promoting photocarrier collection in the natural region can provide measurable improvements toward realizing high-efficient PEC H_2O_2 production.

Constructing an internal electric field in the natural region as an additional driving force is critical to promote photocarriers collection.[12] So far, various strategies have been widely employed to build an electric field, such as surface tailoring,[13] heterojunction,[14,15] and facet junction.[16,17] However, the influence of these electric fields is mostly spatially limited to the surface or depletion area, rarely modulating the recombination process in the field-free region.[15,18,19] The depolarization field is a typical way to promote charge separation in both bulk and surface, while it is confined to ferroelectrics.[20,21] Thus, a universal approach to construct full-space electric field through the photoelectrode is the remedial approach to inhibit carrier recombination.

Gradient homojunction provides an alternative approach to creating a full-space electric field, which is often employed in multijunction photovoltaic devices, like CuInGaSe (CIGS) solar cells.[22] In these devices semiconductors with equal band gaps but different Fermi levels are placed in contact.[23,24] Compared to heterojunctions, homojunctions have the following advantages: (1) easier to prepare since only a single semiconductor material is required; (2) same material with less lattice mismatch is beneficial to mitigate interfacial defects. For instance, Berglund and co-workers developed a gradient self-doped $CuBi_2O_4$ photocathode with forward electric field to achieve a charge separation efficiency of 34%.[25,26] Therefore, gradient homojunction depends on a fine modulation of the semiconductors' Fermi level, which is challenging to achieve

Received: August 3, 2022
Accepted: September 16, 2022

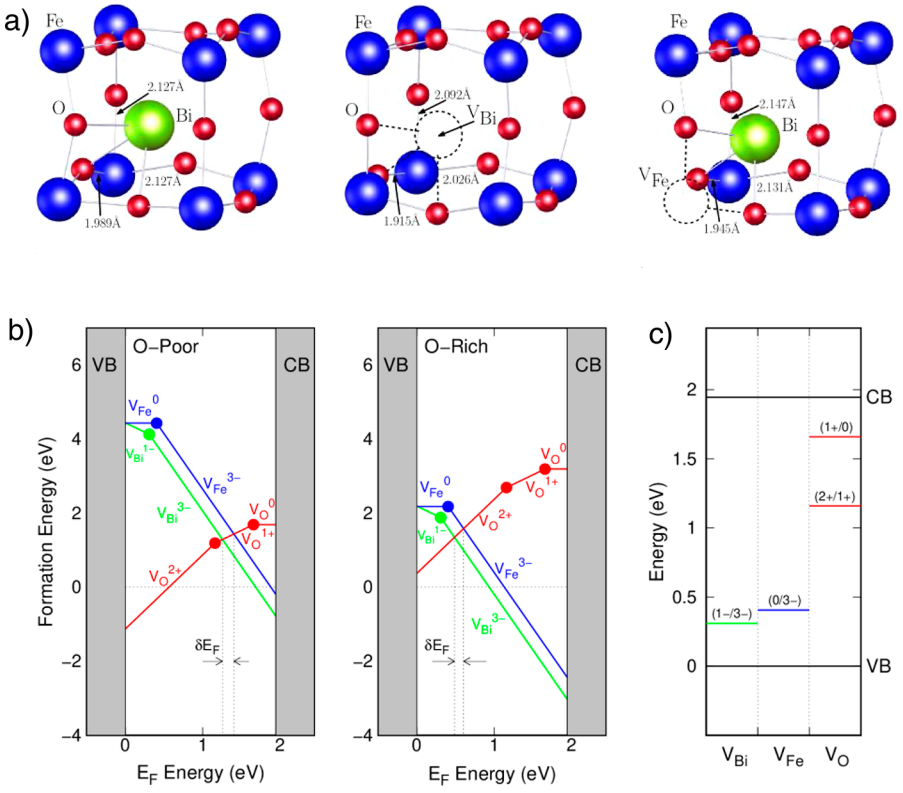

Figure 1. Local structure for pristine BFO, Fe vacancy, and Bi vacancy (a); formation energies for neutral and charged Bi, Fe, O vacancies (b); and defect transition levels (c).

without a deeper understanding of materials' electronic structure.

In this work, a full-space electric field was induced in $BiFeO_3$ (denoted as BFO) films by constructing a gradient homojunction through Fermi level engineering. First-principles calculations reveal that the Fermi level of BFO depends on the density of Fe and Bi vacancies in the film, which are shallow acceptors to define the p-type conductivity of BFO. These results were validated by surface potential and ultraviolet photoelectron spectroscopy (UPS) analysis. PEC performances of BFO films, including current–voltage (J–V) response and H_2O_2 production activity, confirm enhanced performance for the forward gradient doped photocathode. Incident and absorbed photon-to-current efficiency (IPCE and APCE) and surface photovoltage (SPV) analysis proved that the enhanced performance is primarily attributed to the improved charge collection efficiency. Thus, this work demonstrated the successful inhibition of photocarrier recombination by gradient homojunction which can be broadly applied to other optoelectronic systems.

Insight into the structural and electronic properties of Bi and Fe vacancy defects and their effect on the Fermi level energy of BFO was obtained by means of density functional theory (DFT) based first-principles calculations at the DFT+U level of theory. Band structure and total density of states calculations for the $R3c$ phase structure of BFO (Figure S1a,b) predict a band gap of 1.95 and 2.30 eV for Hubbard U values of 3.0 and 4.5 eV, respectively, in line with previous results and in good agreement with measured optical gaps of 2.10–2.86 eV.[27−31] Point defects are calculated for U = 3.0 eV level of theory using the supercell method (see Supporting Information) for ease of comparison with previous DFT results.[27−31] Tables S1–S3 report computed chemical potentials and formation energies for neutral defects. Neutral and charged Fe and Bi vacancies distort the local geometry of the $R3c$ polar structure. For charged vacancies, V_{Fe}^{3-} and V_{Bi}^{3-}, bond lengths are slightly modified around the vacancy with respect to the pristine structure (Figure 1a). The additional negative charge of the defects reproduces the charge provided by Fe and Bi to the crystal and therefore promote their stability. The stability of Bi, Fe, and O vacancies is further studied by computing formation energies as a function of the Fermi energy (Figure 1b).[32] For O-poor and O-rich conditions, Fe and Bi vacancies both act as shallow acceptors, with Bi vacancies more stable than Fe vacancies. Oxygen vacancies act as donors, as shown by the defect transition levels (Figure 1c). Our results are in good qualitative agreement with previous first-principles results using different levels of theory.[27−31]

Notably, the position of the Fermi level is greatly affected by the stability of O vacancies, suggesting that growth conditions greatly modulate the Fermi level position. Different experimental Bi:Fe ratios for BFO are modeled using our theoretical results for isolated point defects. For the case of Bi:Fe ratio of 1:0.95 in growth solution (see below), Fe vacancies are expected to be dominant in the solid. Hence, in this case, the Fermi level is estimated as the intersection between the formation energies of V_{Fe}^{3-} and V_O vacancies. In this case, the Fermi level is set at 1.40 eV for O-poor conditions and at 0.61 eV for O-rich conditions, as shown in Figure 1b (δE_F). Similarly, for the case of Bi:Fe ratio of 0.95:1, where Bi vacancies are dominant, the Fermi level is set at 1.26 and 0.49 eV for O-poor and O-rich conditions, respectively. Therefore, our results suggest that the Fermi level can be modulated

https://doi.org/10.1021/acsenergylett.2c01750
ACS Energy Lett. XXXX, XXX, XXX–XXX

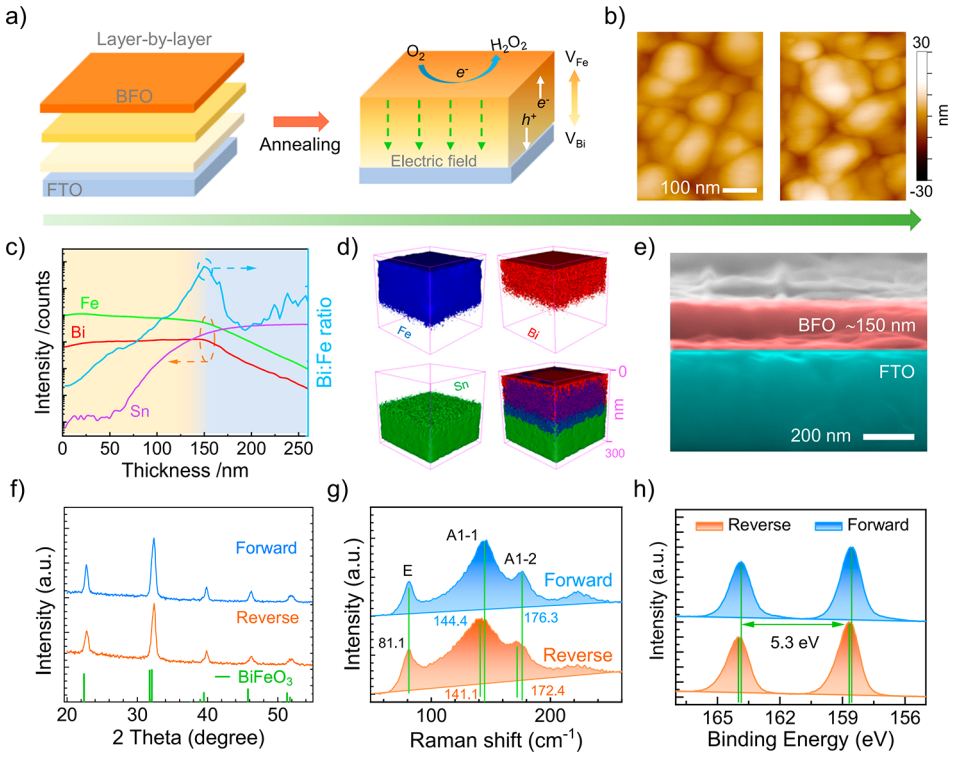

Figure 2. Schematic illustration of the fabrication procedure for gradient doped films (a); plane-view AFM images of the gradient doped films, forward (left) and reverse (right) (b); TOF-SIMS depth profile of the thin film composition (c); TOF-SIMS 3D element distribution of Fe, Bi, Sn and the overlay (d) in the gradient BFO film; the cross-section SEM image of BFO films (e); the XRD pattern (f), Raman spectra (g) and XPS core-level spectra of gradient BFO films (h).

(through Fe and Bi vacancies) in the ranges indicated by δE_F in Figure 1b. Our results are qualitatively similar for different values of the Hubbard U and hybrid functionals.

We can further estimate the position of the Fermi level as a function of O vacancy concentration by solving the electroneutrality equation for charge balance.[33] We use arbitrary defect concentrations for Fe and Bi vacancy and the transition levels obtained from DFT as input parameters. Figure S1c shows our results for the extreme cases of 5% of Fe and Bi vacancies. In both cases, the Fermi level changes from p-type at O-rich to n-type under O-poor conditions, in agreement with the results of Figure 1b.

The above mechanistic insights leveraged a path to build a BFO film with continues homojunction through modulating Bi and Fe vacancies. As shown in Figure 2a, the gradient self-doped BFO films were fabricated using a three-step spin-coating and annealing process. Typically, for a forward gradient BFO film (defined as the V_{Fe} at the surface and at V_{Bi} the bottom), the lower Bi:Fe mole ratio (0.95:1, V_{Bi} dominated) precursor was used for the first two spin-coating cycles, then the moderate ratio (1:1) precursor for the following two cycles, and finally the higher ratio (1:0.95, V_{Fe} dominated) for the last two cycles. After that, the films were annealed at 600 °C for 1 h to improve the diffusion of Bi and Fe vacancies in films. The reversed gradient BFO film is fabricated using the same method but with a lower Bi:Fe ratio precursor introduced first. Plan-view AFM images of the resultant film revealed a homogeneous, compact layer with granular morphology and uniform grain size of around 50−200 nm. As shown in Figure 2b, the forward and reverse doped films show identical morphology.

Gradient distribution of Bi and Fe through the thickness of the BFO film was investigated by time-of-flight secondary ion mass spectrometry (TOF-SIMS).[33] In the depth profile (Figure 2c) of the gradient BFO film, the Fe concentration monotonically decreased from the surface to 150 nm in depth, while the Bi concentration increased and then dramatically decreased. As a result, the Bi:Fe ratio continuously increased from the surface to 150 nm depth in the bulk. In Figure 2d, the 3D element distribution images indicate layered structure and the uniform spatial distribution of BFO film horizontally on the FTO substrate. The cross-section scanning electron microscopy (SEM) image in Figure 2e further confirmed the layered structure of prepared films with BFO thickness of around 150 nm.

X-ray diffraction (XRD) patterns of BFO films, in Figure 2f, illustrates that all sharp and strong diffraction peaks are well-matched to those of $BiFeO_3$ (JCPDS 86-1518) with good crystallinity. Moreover, the well-matched diffraction peaks of homogeneous BFO films with varied V_{Bi} and V_{Fe} density in Figure S2 implies the excellent phase purity and defects tolerance of BFO films. Likewise, Raman spectra shown in Figure 2g are indicative of phase-pure BFO. Meanwhile, slight shifts can be found for the A1-1 and A1-2 signals, which are probably due to vacancies caused lattice distortion.[34] The X-ray photoelectron spectroscopy (XPS) in Figure 2h also displays a binding energy shift in gradient doped films. The Bi and Fe core-level spectra of the reverse BFO film show a higher binding energy shift compared with the forward BFO film (Figure 2h and Figure S3). Considering the forward film has higher V_{Fe} density at the surface than the reverse film, the shift could generally be attributed to the increase of equilibrium electron density and hence the binding energy.[35,20] Thus,

https://doi.org/10.1021/acsenergylett.2c01750
ACS Energy Lett. XXXX, XXX, XXX−XXX

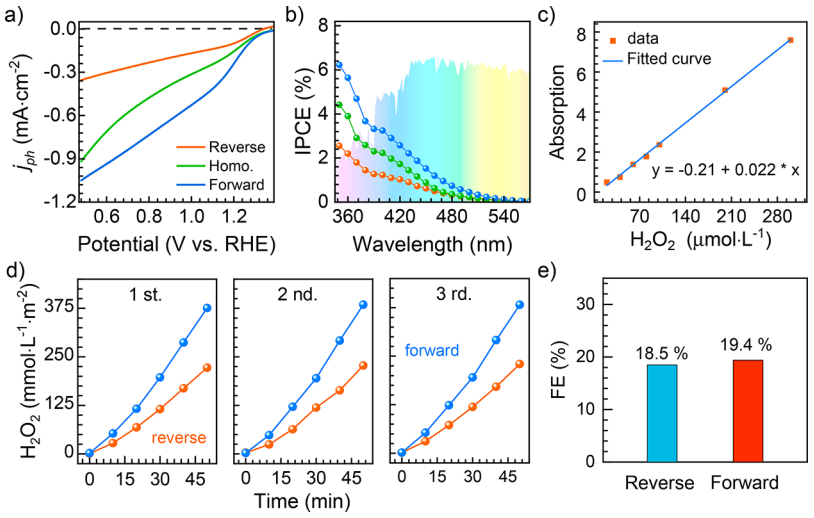

Figure 3. *J*–*V* responses of the reverse, homogeneous, and forward gradient BFO films under blue LED (430 nm, 60 mW·cm^{-2}) illumination in 0.1 M $KHCO_3$ with 0.1 M $Na_2S_2O_8$ (pH 8.2) as an electron scavenger (a); IPCE spectra of BFO photocathodes at 0.58 V vs RHE (b); standard curve of H_2O_2 detection (c); PEC H_2O_2 production activities (d) and FE (e) for H_2O_2 production in $KHCO_3$ solution.

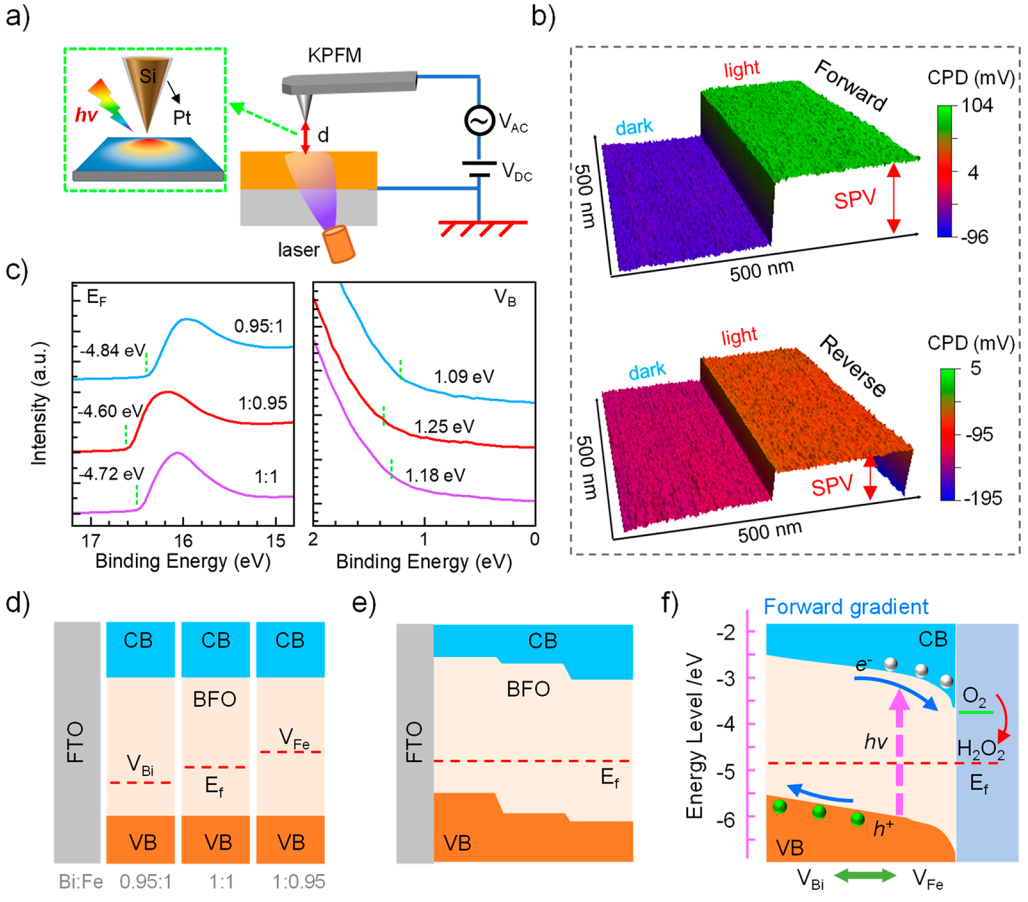

Figure 4. Schematic illustration of the SPV setup (a); CPD maps of the forward and reverse gradient BFO films under blue dark or LED light illumination (b); UPS Fermi level and valence band edge of BFO films (c); schematic band alignments of BFO films before contact (d) and after contact (e), and the formed full-space electric field (f).

taking the above results together, we claim successful fabrication of the gradient BFO films. As the emphasis of this work is to investigate the effect of gradient doping on the optoelectronic properties of BFO films, we elected to carefully evaluate and compare the forward and reversed gradient doped films to uncover the specific origins of these observations through a suite of characterization methods.

In assessing the BFO films as photocathodes, the performance was evaluated using standard three-electrodes system under blue LED (430 nm) illumination at 60 mW·cm^{-2} in 0.1 M $KHCO_3$ solution. An electron scavenger (0.1 M, $Na_2S_2O_8$)

https://doi.org/10.1021/acsenergylett.2c01750
ACS Energy Lett. XXXX, XXX, XXX−XXX

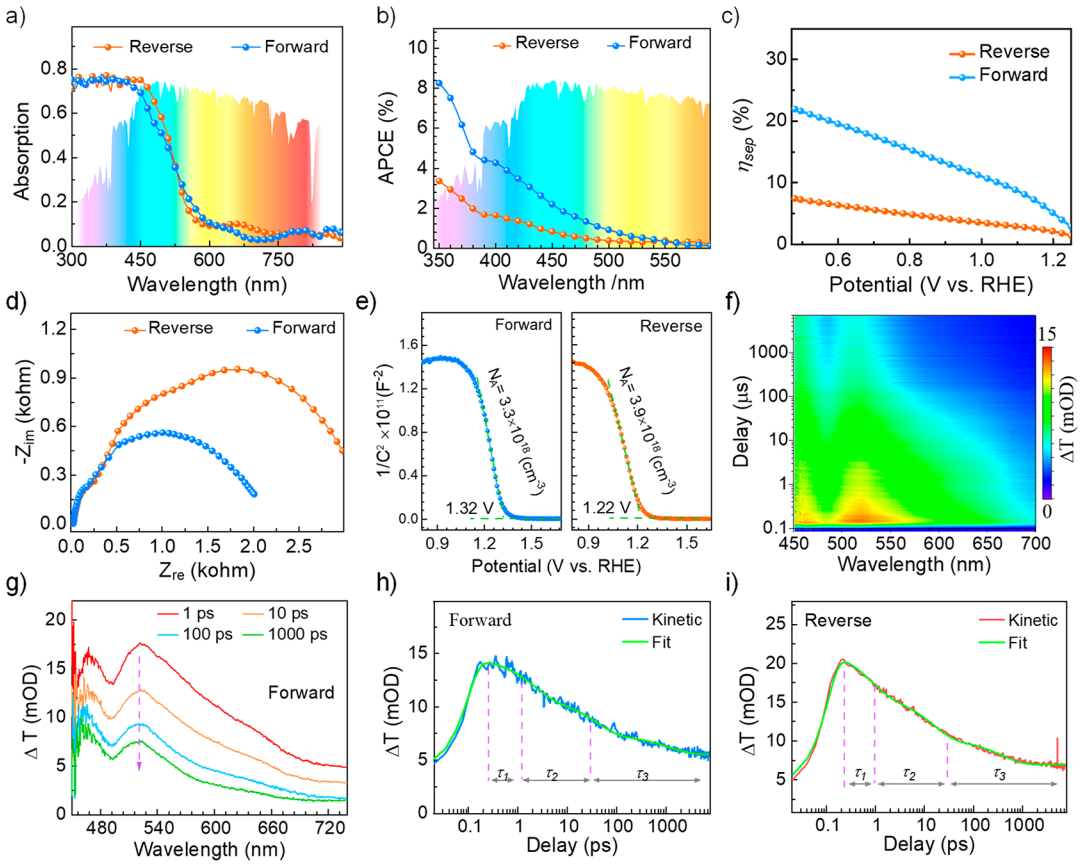

Figure 5. UV−vis absorption spectra (a), calculated APCE spectra (b), and the charge separation efficiency (c) of prepared BFO photocathodes; EIS plots of BFO films measured at 0.68 V vs RHE under blue LED illumination (d); Mott−Schottky plots of BFO films at 2 kHz (e); contour maps of transient transmission spectrum of forward gradient BFO film in the range of −100 fs to 7.4 ns (f); representative transmission spectra of forward gradient BFO film at various pump−probe delays (g); transient transmission decay and related fitting curves of forward (h) and reverse (i) doped BFO films in the range of −100 fs to 7.4 ns. Excitation wavelength: 400 nm. Power: 1.5 μJ per pulse. Beam diameter: 0.3 mm.

was added to the electrolyte to study the intrinsic properties of photocathodes without the influence of surface activity. Figure 3a shows the $J-V$ responses of homogeneous, forward, and reverse gradient doped BFO films. The forward BFO film exhibits the best PEC performance: a 16% increase in the photocurrent to −1.02 mA·cm^{-2} at 0.5 V vs RHE and a 26% improvement in the fill factor when compared with the homogeneous BFO film (−0.88 mA cm^{-2} at 0.5 V vs RHE). The reverse gradient doped photocathode shows a negative influence with photocurrent of only 40% of the homogeneous BFO film. To further support defects modulated PEC performance, three homogeneous BFO films with Bi:Fe mole ratios of 1:0.95, 1:1, and 0.95:1 were prepared and evaluated (Figure S4). The photocurrent significantly enhanced about three times from −0.29 mA cm^{-2} to −0.88 mA cm^{-2} at 0.5 V vs RHE as the Bi:Fe ratio varied from 1:0.95 to 0.95:1. The onset potential also displays a positive shift from 1.25 to 1.38 V vs RHE (taken at −10 μA cm^{-2}). Details of $J-V$ response were summarized in Table S4. Incident photon-to-current conversion efficiency (IPCE) further confirmed the enhanced PEC performance through forward gradient doping. As shown in Figure 3b, forward gradient doping barely changes the onset wavelength of BFO films (550 nm) but improves the IPCE value by 43%.

PEC performance was further evaluated by testing the H_2O_2 production activity in a homemade two-compartment cell as illustrated in Figure S5. The BFO photocathode and counter electrode were separated by a Nafion membrane. The electrolyte was 0.1 M $KHCO_3$ solution and purged with O_2 (99.9%) gas for 30 min before and during the measurement. Figure 3c shows the standard curve of H_2O_2 detection with excellent linear correlation. Figure 3d displays the production of H_2O_2 as a function of time under AM 1.5 irradiation at an applied bias of 0.6 V vs RHE. The corresponding $I-t$ curve is available in Figure S6. Constant with $J-V$ responses, the forward gradient doped BFO photocathode exhibited better performance with an average H_2O_2 concentration of around 380 mmol·(L·m^2)$^{-1}$ within 50 min, about 1.7 times higher than the reverse gradient doped BFO (90.6 mmol·(L·m^2)$^{-1}$). Additionally, recyclability tests revealed that the system could be used for stable H_2O_2 generation for three cycles without significant decay (Figure 3d). Finally, the faradic efficiency (FE) was calculated based on the equation described in the Supporting Information. As shown in Figure 3e, the similar FE with an average value of 19% indicates that gradient doping rarely influences the reaction selectivity. However, the low FE of BFO films indicates that a highly efficient cocatalyst is a critical need, which may be investigated in the following work.[1,36,37] In summary, the forward gradient doped BFO films show the best PEC performance both in $J-V$ response and H_2O_2 production activity.

https://doi.org/10.1021/acsenergylett.2c01750
ACS Energy Lett. XXXX, XXX, XXX−XXX

The constructed full-space electric field corresponds to the enhanced PEC performance, as identified by Fermi level analysis, including surface potential and ultraviolet photoelectron spectroscopy (UPS).[13] Figure 4a displays the schematic illustration of SPV setup, which is based on Kelvin probe force microscopy (KPFM) and light illumination system.[38−40] For data collection, the film was illuminated from the back side with an LED light source and through optical fiber. Figure S7a illustrated the origin of the contact potential difference (CPD). Under illumination, photogenerated minority carriers will shift the Fermi level upward at the interface and the resulting average potential difference (ΔCPD) in the dark and under illumination is defined as the surface photovoltage (SPV). Figure 4b and Figure S7b show the CPD maps and plots through BFO films. In the dark, the reverse gradient BFO has significantly lower CPD (approximately −126 mV) than the forward gradient BFO (approximately −85 mV), indicating that reverse BFO has a larger work function than the forward BFO at the surface. Under illumination, both films show clear enhanced CPD, and the SPV of forward BFO is nearly three times as large as that of reverse BFO. Since the SPV is mainly determined by the density of photogenerated minority carriers (electrons in p-type BFO), such an enhanced SPV indicates that the forward gradient is beneficial for photocarriers' separation. UPS results further confirmed the V_{Bi} and V_{Fe} adjusted Fermi level and valence band (VB) edge position of BFO films. As shown in Figure 4c, the work function of BFO films significantly increased from 4.60 to 4.84 eV, and the distance between the Fermi level and VB edge decreased from 1.25 to 1.09 eV, as the V_{Bi} concentration increased. These results matched well with first-principles analysis and confirmed the V_{Bi} and V_{Fe} as acceptors to modulate the position of the Fermi level.

Altogether, our results illustrate how the gradient V_{Bi} and V_{Fe} and the resulting gradient of Fermi level lead to an internal electric field. Before contact, BFO films with different vacancies density possess different Fermi levels, as shown in Figure 4d. After contact, the Fermi level will equilibrate by redistributing the free carriers between the different regions so that the CB and VB bend at each interface, as illustrated by Figure 4e. A forward gradient BFO photocathode will contain a full-space electric field shown in Figure 4f, which would promote photocarrier separation by field-enhanced diffusion (drift) of the photogenerated electrons toward the BFO/electrolyte interface and drift of photogenerated holes toward the back contact.

The full-space electric field through the film will have an influence on the carrier dynamics of semiconductors. To verify it, other effects should be excluded through suitable characterizations. First, light-harvesting capacities of gradient doped films have been measured and compared. As shown in Figure 5a, the direction of gradient doping barely influences the light-harvesting capacity of BFO films. Additionally, absorbed photon-to-current conversion efficiency (APCE, Figure 5b) calculated from IPCE and related UV−vis spectrum shows a similar improvement trend as that of IPCE (Figure 3b), indicating that the enhanced PEC performance with forward gradient doping is mainly attributed to improved charge carrier separation and transport. This enhancement was further confirmed by the calculated charge separation efficiency. As shown in Figure 5c, the forward gradient doped photocathode shows a significant improvement of η_{sep}, 3 times larger than that of the reversed one.

Electrochemical impedance spectroscopy (EIS) plots in Figure 5d indicate that the forward gradient doped BFO film shows better charge transport capacity than the reverse BFO film, as proved by the significantly reduced charge transport resistance. Moreover, Mott−Schottky analysis (Figure 5e) indicates that the flat-band potential (E_{fb}) of BFO films was significantly modified by the gradient self-doping process. As summarized in Table S1, the E_{fb} of forward gradient BFO film is a round 1.32 V vs RHE, 100 mV larger than that of reversed gradient film (1.22 V vs RHE). Such a positive shift of the E_{fb} is a direct evidence of the Fermi level shifting toward the VB edge. The similar carrier density in the films indicates that forward or reversed gradient does not affect the overall carrier density in the film.

Figure 5f and Figure S8a show the transmission contour maps of BFO film that contain two main peaks located at 460 nm (2.65 eV) and 520 nm (2.38 eV) which decrease over time. These peaks are attributed to the ligand-to-metal charge transition between O-to-Bi (2.27 eV) and O-to-Fe (1.82 eV).[15] Figure 5g and Figure S8b are the transmission spectra extracted from the contour maps of BFO films in the visible region at different delay times. The ratio changes in BFO films rarely influence the sharpness of spectra. It should be noted that the sharp signals from thin film semiconductors are related to a modification of the optical properties (the complex index of refraction) of the semiconductor as a result of the perturbation of the charge carrier band population by the pump pulse according to eq 1,[32,41−44]

$$\Delta n(N, P, \lambda) = -\left(\frac{e^2\lambda^2}{8\pi^2 c^2 \varepsilon_0 n}\right)\left(\frac{\Delta N}{m_e} + \frac{\Delta P}{m_h}\right) \quad (1)$$

where Δn is the change of complex refractive index; ΔN and ΔP are the photogenerated electrons and holes density; λ is the wavelength of incident light; c is the speed of photons in vacuum; m_e and m_h are the effective mass of electrons and holes.

The carrier lifetimes of BFO films were extracted from reflection decay, as shown in Figure 5h,i. The kinetic traces at 520 nm with 400 nm excitation were well fitted via eq 2:

$$\Delta A(t) = k_1 e^{-t/\tau_1} + k_2 e^{-t/\tau_2} + k_3 e^{-t/\tau_3} \quad (2)$$

where τ_1, τ_2, and τ_3 are time constants and k_1, k_2, and k_3 are weightings (amplitudes). The first time constant (τ_1) is related to hot carrier cooling through carrier−carrier scattering and momentum relaxation, which is commonly less than 1 ps. The second time constant (τ_2) is associated with energy relaxation involving carrier-phonon scattering. The third time constant is attributed to the trapping and recombination of charge carriers.[45−47] The final carrier lifetime was calculated by summing these three time constants with weights. Table S5 shows the fitting parameters of BFO films. The total carrier lifetime of forward BFO film (201 ps) is almost 1.3 times as large as that of reversed film (153 ps), which further indicates that the forward gradient doping is an efficient approach to prolong the carrier lifetime and inhabit carrier recombination. Thus, we conclude that the full-space electric field through the BFO films improved PEC performance by enhanced carrier dynamics, including improved charge separation, transport, and prolonged lifetime.

In summary, a BFO-based photocathode with improved photocarriers collection was achieved by constructing a full-space electric field through the film. First-principles calcu-

https://doi.org/10.1021/acsenergylett.2c01750
ACS Energy Lett. XXXX, XXX, XXX−XXX

lations revealed that Fe vacancies act as acceptor impurities in BFO, which can modulate the Fermi level. TOF-SIMS depth profile and XPS analysis showed the gradient distribution of Fe vacancies within BFO films and illustrated that its concentration can be modified by varying the Fe ratio in the precursor. The $J-V$ response and H_2O_2 production tests show clearly enhanced PEC performance by forward gradient doping, which improved the photocurrent by 2 times, the onset potential by 130 mV, and H_2O_2 production by 69%, compared to the reverse gradient doping approach. SPV and UPS analyses show the modified Fermi level and reveal the construction of gradient homojunction and full-space electric field. EIS, Mott−Schottky, and transient spectroscopy analyses indicate the forward full-space electric field as additional driving force that significantly promoted photocarriers collection and prolonged carriers' lifetime. These results demonstrate that deeper understanding of electric structures of materials and constructing full-space electric field through gradient self-doping are a viable approach to promote photocarriers collection, which deserves great attention and wide applications.

■ ASSOCIATED CONTENT

Supporting Information

The Supporting Information is available free of charge at https://pubs.acs.org/doi/10.1021/acsenergylett.2c01750.

Detailed experimental section, maximum photocurrent, XPS spectra, SEM images, EDX map, $J-V$ response, optical photos, Tauc plot, and band energy diagram (PDF)

■ AUTHOR INFORMATION

Corresponding Authors

Sebastian E. Reyes-Lillo − *Departamento de Ciencias Físicas, Universidad Andres Bello, Santiago 837-0136, Chile*; Email: sebastian.reyes@unab.cl

Yanbo Li − *Institute of Fundamental and Frontier Sciences, University of Electronic Science and Technology of China, Chengdu 610054, China*; orcid.org/0000-0002-3017-762X; Email: yanboli@uestc.edu.cn

Zemin Zhang − *School of Physical Science and Technology, Lanzhou University, Lanzhou 730000, China*; orcid.org/0000-0001-8293-391X; Email: zhangzemin@lzu.edu.cn

Authors

Bing Tan − *School of Physical Science and Technology, Lanzhou University, Lanzhou 730000, China*

Abdul M. Reyes − *Departamento de Ciencias Físicas, Universidad Andres Bello, Santiago 837-0136, Chile; Centro de Excelencia en Nuevos Materiales (CENM) y Departamento de Física, Grupo de Óptica Cuántica, Universidad del Valle, 25360 Santiago de Cali, Colombia*

Eduardo Menéndez-Proupin − *Departamento de Física Aplicada I, Escuela Politécnica Superior, Universidad de Sevilla, Seville E-41011, Spain*; orcid.org/0000-0001-7534-8464

Complete contact information is available at: https://pubs.acs.org/10.1021/acsenergylett.2c01750

Notes

The authors declare no competing financial interest.

■ ACKNOWLEDGMENTS

We acknowledge the scientific and technical input and support from the School of Physical Science and Technology, Lanzhou University (China). This work was financially supported by the Supporting Fund for Young Researchers from Lanzhou University, Science and Technology Foundation for Youths of Gansu Province (Grant 20JR10RA643). A.M.R. acknowledges support from ANID FONDECYT Postdoctorado Grant 3220460 and Fondo Nacional de Financiamiento para la Ciencia la Tecnología y la Innovación "Francisco José de Caldas" de MINCIENCIAS y la Universidad del Valle. S.E.R.-L acknowledges support from ANID FONDECYT Regular Grant 1220986. Theory work was performed at The Molecular Foundry, which is supported by the Office of Science, Office of Basic Energy Sciences of the U.S. Department of Energy under Contract DE-AC02-05CH11231. Powered@NLHPC: This research was partially supported by the supercomputing infrastructure of NLHPC (Grant ECM-02).

■ REFERENCES

(1) Gao, R.; Pan, L.; Li, Z.; Shi, C.; Yao, Y.; Zhang, X.; Zou, J. J. Engineering Facets and Oxygen Vacancies over Hematite Single Crystal for Intensified Electrocatalytic H_2O_2 Production. *Adv. Funct. Mater.* **2020**, *30* (24), 1910539.

(2) Liu, T.; Pan, Z.; Vequizo, J. J. M.; Kato, K.; Wu, B.; Yamakata, A.; Katayama, K.; Chen, B.; Chu, C.; Domen, K. Overall Photosynthesis of H_2O_2 by An Inorganic Semiconductor. *Nat. Commun.* **2022**, *13* (1), 1034.

(3) Liu, J.; Zou, Y.; Jin, B.; Zhang, K.; Park, J. H. Hydrogen Peroxide Production from Solar Water Oxidation. *ACS Energy Lett.* **2019**, *4* (12), 3018−3027.

(4) Cheng, W.-H.; de la Calle, A.; Atwater, H. A.; Stechel, E. B.; Xiang, C. Hydrogen from Sunlight and Water: A Side-by-Side Comparison between Photoelectrochemical and Solar Thermochemical Water-Splitting. *ACS Energy Lett.* **2021**, *6* (9), 3096−3113.

(5) Li, C.; He, J.; Xiao, Y.; Li, Y.; Delaunay, J.-J. Earth-Abundant Cu-Based Metal Oxide Photocathodes for Photoelectrochemical Water Splitting. *Energy Environ. Sci.* **2020**, *13* (10), 3269−3306.

(6) Piekner, Y.; Ellis, D. S.; Schleuning, M.; Grave, D. A.; Schnell, P.; Dotan, H.; Abdi, F.; Rothschild, A. External Quantum Efficiency Spectra of $BiVO_4$ Thin Film Photoanodes under Bias Illumination. *J. Electrochem. Soc.* **2022**, *169*, 046513.

(7) Piekner, Y.; Ellis, D. S.; Grave, D. A.; Tsyganok, A.; Rothschild, A. Wasted Photons: Photogeneration Yield and Charge Carrier Collection Efficiency of Hematite Photoanodes for Photoelectrochemical Water Splitting. *Energy Environ. Sci.* **2021**, *14*, 4584−4598.

(8) Zhang, K.; Lu, Y.; Zou, Q.; Jin, J.; Cho, Y.; Wang, Y.; Zhang, Y.; Park, J. H. Tuning Selectivity of Photoelectrochemical Water Oxidation via Facet-Engineered Interfacial Energetics. *ACS Energy Lett.* **2021**, *6* (11), 4071−4078.

(9) Segev, G.; Jiang, C.-M.; Cooper, J. K.; Eichhorn, J.; Toma, F. M.; Sharp, I. D. Quantification of the Loss Mechanisms in Emerging Water Splitting Photoanodes through Empirical Extraction of the Spatial Charge Collection Efficiency. *Energy Environ. Sci.* **2018**, *11* (4), 904−913.

(10) Gottesman, R.; Peracchi, I.; Gerke, J. L.; Irani, R.; Abdi, F. F.; van de Krol, R. Shining a Hot Light on Emerging Photoabsorber Materials: The Power of Rapid Radiative Heating in Developing Oxide Thin-Film Photoelectrodes. *ACS Energy Lett.* **2022**, *7* (1), 514−522.

(11) Jiang, X.; Cheng, X.; Zhang, Z.; Chen, T.; Tao, K.; Han, W. Computation-Assisted Performance Optimization for Photoelectrochemical Photoelectrodes. *Appl. Phys. Lett.* **2022**, *120* (6), 063901.

(12) Zhang, S.; Wang, J.; Wen, S.; Jiang, M.; Xiao, H.; Ding, X.; Wang, N.; Li, M.; Zu, X.; Li, S.; Yam, C.; Huang, B.; Qiao, L. Approaching Charge Separation Efficiency to Unity without Charge Recombination. *Phys. Rev. Lett.* **2021**, *126* (17), 176401.

(13) Zhang, Z.; Lindley, S. A.; Guevarra, D.; Kan, K.; Shinde, A.; Gregoire, J. M.; Han, W.; Xie, E.; Haber, J. A.; Cooper, J. K. Fermi Level Engineering of Passivation and Electron Transport Materials for p-Type $CuBi_2O_4$ Employing a High-Throughput Methodology. *Adv. Funct. Mater.* **2020**, *30* (24), 2000948.
(14) Zhang, Z.; Lindley, S. A.; Dhall, R.; Bustillo, K.; Han, W.; Xie, E.; Cooper, J. K. Beneficial CuO Phase Segregation in the Ternary p-Type Oxide Photocathode $CuBi_2O_4$. *ACS Appl. Energy Mater.* **2019**, *2* (6), 4111−4117.
(15) Zhang, Z.; Tan, B.; Ma, W.; Liu, B.; Sun, M.; Cooper, J. K.; Han, W. $BiFeO_3$ Photocathodes for Efficient H_2O_2 Production via Charge Carrier Dynamics Engineering. *Mater. Horiz.* **2022**, *9*, 1999−2006.
(16) Tan, B.; Liu, B.; Sun, M.; Li, Y.; Cao, Z.; Zhang, Z. Enhanced Charge Collection and Surface Activity of a $CuBi_2O_4$ Photocathode via Crystal Facet Engineering. *J. Mater. Chem. A* **2022**, *10* (17), 9427−9434.
(17) Li, R.; Zhang, F.; Wang, D.; Yang, J.; Li, M.; Zhu, J.; Zhou, X.; Han, H.; Li, C. Spatial Separation of Photogenerated Electrons and Holes Among {010} and {110} Crystal Facets of $BiVO_4$. *Nat. Commun.* **2013**, *4*, 1432.
(18) Sun, M.; Liu, B.; Han, W.; Zhang, Z.; Xie, M. $CuBi_2O_4$ Photocathode with Integrated Electric Field for Enhanced H_2O_2 Production. *Appl. Catal., B* **2022**, *304*, 120980.
(19) Liu, B.; Sun, M.; Tan, B.; Zhang, Z.; Han, W. Enhanced Photocarrier Collection in Bismuth Vanadate Photoanode through Modulating the Inner Potential Distribution. *Adv. Opt. Mater.* **2022**, *10*, 2200046.
(20) Tian, Y.; Wang, A.; Wei, Y.; Pei, M.; Cao, R.; Gu, Z.; Yuan, Q.; Hu, Y.; Wang, J.; Liu, K.; Shang, D.; Niu, J.; An, X.; Long, R.; Zhang, J. Large-Area Printing of Ferroelectric Surface and Super-Domain for Solar Water Splitting. *Adv. Funct. Mater.* **2022**, *32*, 2111180.
(21) Tian, Y.; Wei, L.; Zhang, Q.; Huang, H.; Zhang, Y.; Zhou, H.; Ma, F.; Gu, L.; Meng, S.; Chen, L. Q.; Nan, C. W.; Zhang, J. Water Printing of Ferroelectric Polarization. *Nat. Commun.* **2018**, *9* (1), 3809.
(22) Choi, P.-P.; Cojocaru-Mirédin, O.; Wuerz, R. Compositional Gradients and Impurity Distributions in $CuInSe_2$ Thin-Film Solar Cells Studied by Atom Probe Tomography. *Surf. Interface Anal.* **2012**, *44* (11−12), 1386−1388.
(23) Zhang, H.; Li, D.; Byun, W. J.; Wang, X.; Shin, T. J.; Jeong, H. Y.; Han, H.; Li, C.; Lee, J. S. Gradient Tantalum-Doped Hematite Homojunction Photoanode Improves Both Photocurrents and Turn-on Voltage for Solar Water Splitting. *Nat. Commun.* **2020**, *11* (1), 4622.
(24) Mirzaei, A.; Eddah, M.; Roualdes, S.; Ma, D.; Chaker, M. Multiple-Homojunction Gradient Ntrogen Doped TiO_2 for Photocatalytic Degradation of Sulfamethoxazole, Degradation Mechanism, and Toxicity Assessment. *Chem. Eng. J.* **2021**, *422*, 130507.
(25) Wang, F.; Septina, W.; Chemseddine, A.; Abdi, F. F.; Friedrich, D.; Bogdanoff, P.; van de Krol, R.; Tilley, S. D.; Berglund, S. P. Gradient Self-Doped $CuBi_2O_4$ with Highly Improved Charge Separation Efficiency. *J. Am. Chem. Soc.* **2017**, *139*, 15094−15103.
(26) Xiao, Y.; Feng, C.; Fu, J.; Wang, F.; Li, C.; Kunzelmann, V. F.; Jiang, C.-M.; Nakabayashi, M.; Shibata, N.; Sharp, I. D.; Domen, K.; Li, Y. Band Structure Engineering and Defect Control of Ta_3N_5 for Efficient Photoelectrochemical Water Oxidation. *Nat. Catal.* **2020**, *3* (11), 932−940.
(27) Paudel, T. R.; Jaswal, S. S.; Tsymbal, E. Y. Intrinsic Defects in Multiferroic $BiFeO_3$ and Their Effect on Magnetism. *Phys. Rev. B* **2012**, *85*, 104409.
(28) Shimada, T.; Matsui, T.; Xu, T.; Arisue, K.; Zhang, Y.; Wang, J.; Kitamura, T. Multiferroic nature of intrinsic point defects in $BiFeO_3$: A hybrid Hartree-Fock density functional study. *Phys. Rev. B* **2016**, *93* (17), 174107.
(29) McDonnell, K. A.; Wadnerkar, N.; English, N. J.; Rahman, M.; Dowling, D. Photo-active and Optical Properties of Bismuth Ferrite ($BiFeO_3$): An Experimental and Theoretical Study. *Chem. Phys. Lett.* **2013**, *572*, 78−84.
(30) Geneste, G.; Paillard, C.; Dkhil, B. Polarons, Vacancies, Vacancy Associations, and Defect States in Multiferroic $BiFeO_3$. *Phys. Rev. B* **2019**, *99* (2), 024104.
(31) Lee, J.; Nahm, H.-H.; Kim, Y.-H. Diversity of Hole-Trap Centers Due to Small Polarons and Bipolarons in Ca-doped $BiFeO_3$: Origin of Electrochromism. *Phys. Rev. B* **2020**, *101* (1), 014110.
(32) Zhang, Z.; Liu, B.; Quinteros, F.; Zhai, X.; Wang, Q.; Han, W.; Xie, E.; Reyes-Lillo, S. E.; Cooper, J. K. Understanding the Role of Oxygen and Hydrogen Defects in Modulating the Optoelectronic Properties of P-Type Metal Oxide Semiconductors. *Chem. Mater.* **2021**, *33* (19), 7829−7838.
(33) Yang, J. H.; Yin, W. J.; Park, J. S.; Ma, J.; Wei, S. H. Review on First-Principles Study of Defect Properties of CdTe as A Solar Cell Absorber. *Semicond. Sci. Technol.* **2016**, *31* (8), 083002.
(34) Jeon, N.; Rout, D.; Kim, I. W.; Kang, S.-J. L. Enhanced Multiferroic Properties of Single-Phase $BiFeO_3$ Bulk Ceramics by Ho Doping. *Appl. Phys. Lett.* **2011**, *98* (7), 072901.
(35) Yang, T.; Wei, J.; Guo, Y.; Lv, Z.; Xu, Z.; Cheng, Z. Manipulation of Oxygen Vacancy for High Photovoltaic Output in Bismuth Ferrite Films. *ACS Appl. Mater. Interfaces* **2019**, *11* (26), 23372−23381.
(36) Zheng, L.; Su, H.; Zhang, J.; Walekar, L. S.; Vafaei Molamahmood, H.; Zhou, B.; Long, M.; Hu, Y. H. Highly Selective Photocatalytic Production of H_2O_2 on Sulfur and Nitrogen co-doped Graphene Quantum Dots Tuned TiO_2. *Appl. Catal., B* **2018**, *239*, 475−484.
(37) Yuan, Q.; Zhao, J.; Mok, D. H.; Zheng, Z.; Ye, Y.; Liang, C.; Zhou, L.; Back, S.; Jiang, K. Electrochemical Hydrogen Peroxide Synthesis from Selective Oxygen Reduction over Metal Selenide Catalysts. *Nano Lett.* **2022**, *22* (3), 1257−1264.
(38) Jiang, Y.; Chen, H. Y.; Li, J. Y.; Liao, J. F.; Zhang, H. H.; Wang, X. D.; Kuang, D. B. Z-Scheme 2D/2D Heterojunction of $CsPbBr_3$/Bi_2WO_6 for Improved Photocatalytic CO_2 Reduction. *Adv. Funct. Mater.* **2020**, *30* (50), 2004293.
(39) Ben, H.; Liu, Y.; Liu, X.; Liu, X.; Ling, C.; Liang, C.; Zhang, L. Diffusion-Controlled Z-Scheme-Steered Charge Separation across PDI/BiOI Heterointerface for Ultraviolet, Visible, and Infrared Light-Driven Photocatalysis. *Adv. Funct. Mater.* **2021**, *31* (37), 2102315.
(40) Woo, G.; Lee, D. H.; Heo, Y.; Kim, E.; On, S.; Kim, T.; Yoo, H. Energy-Band Engineering by Remote Doping of Self-Assembled Monolayers Leads to High-Performance IGZO/p-Si Heterostructure Photodetectors. *Adv. Mater.* **2022**, *34* (6), 2107364.
(41) Xu, Z.; Hou, B.; Zhao, F.; Cai, Z.; Shi, H.; Liu, Y.; Hill, C. L.; Musaev, D. G.; Mecklenburg, M.; Cronin, S. B.; Lian, T. Nanoscale TiO_2 Protection Layer Enhances the Built-In Field and Charge Separation Performance of GaP Photoelectrodes. *Nano Lett.* **2021**, *21* (19), 8017−8024.
(42) Sabbah, A. J.; Riffe, D. M. Femtosecond Pump-probe Reflectivity Study of Silicon Carrier Dynamics. *Phys. Rev. B* **2002**, *66*, 165217.
(43) Prabhu, S. S.; Vengurlekar, A. S. Dynamics of the Pump-probe Reflectivity Spectra in GaAs and GaN. *J. Appl. Phys.* **2004**, *95* (12), 7803−7812.
(44) Cooper, J. K.; Reyes-Lillo, S. E.; Hess, L. H.; Jiang, C.-M.; Neaton, J. B.; Sharp, I. D. Physical Origins of the Transient Absorption Spectra and Dynamics in Thin-Film Semiconductors: The Case of $BiVO_4$. *J. Phys. Chem. C* **2018**, *122* (36), 20642−20652.
(45) Shenje, L.; Larson, S.; Zhao, Y.; Ullrich, S. Composition Effects on Ultrafast Optical Properties of Cu_xO_y Thin Films: A Transient Absorption Study. *J. Phys. Chem. C* **2020**, *124* (45), 24908−24918.
(46) Fischer, M. C.; Wilson, J. W.; Robles, F. E.; Warren, W. S. Invited Review Article: Pump-probe microscopy. *Rev. Sci. Instrum.* **2016**, *87* (3), 031101.
(47) Born, B.; Krupa, J. D. A.; Geoffroy-Gagnon, S.; Hristovski, I. R.; Collier, C. M.; Holzman, J. F. Ultrafast Charge-Carrier Dynamics of Copper Oxide Nanocrystals. *ACS Photonics* **2016**, *3* (12), 2475−2481.

https://doi.org/10.1021/acsenergylett.2c01750
ACS Energy Lett. XXXX, XXX, XXX−XXX